MICROWAVE AND HARD X-RAY OBSERVATIONS OF FOOTPOINT EMISSION FROM SOLAR FLARES

M. R. KUNDU
Dept. of Astronomy, Univ. of Maryland, College Park, MD 20742 USA

N. NITTA
Lockheed Palo Alto Research Laboratory, Palo Alto, CA 94304 USA

S. M. WHITE
Dept. of Astronomy, Univ. of Maryland, College Park, MD 20742 USA

K. SHIBASAKI, S. ENOME
Nobeyama Radio Observatory, Minamisaku-gun, Nagano 384-13, Japan

and

T. SAKAO, T. KOSUGI, and T. SAKURAI
National Astronomical Observatory, Mitaka-shi, Tokyo 181, Japan

ABSTRACT

We investigate radio and X-ray imaging data for two solar flares in order to test the idea that asymmetric precipitation of nonthermal electrons at the two ends of a magnetic loop is consistent with the magnetic mirroring explanation. The events we present were observed in May 1993 by the HXT and SXT X-ray telescopes on the *Yohkoh* spacecraft, and by the Nobeyama 17 GHz radioheliograph. The hard X-ray images in one case show two well-separated sources; the radio images indicate circularly–polarized nonthermal radio emission with opposite polarities from these two sources, indicating oppositely directed fields and consistent with a single-loop model. In the second event there are several sources in the HXT images which appear to be connected by soft X-ray loops. The strongest hard X-ray source has unpolarized radio emission, whereas the strongest radio emission lies over strong magnetic fields and is polarized. In both events the strongest radio emission is highly polarized and not coincident with the strongest hard X-ray emission. This is consistent with asymmetric loops in which the bulk of the precipitation (and hence the X–ray emission) occurs at the weaker-field footpoint.

Subject headings: Sun: X–rays, γ–rays - Sun: radio radiation - Sun: flares

1. INTRODUCTION

A close connection between the energetic electrons emitting microwaves and hard x-rays (HXR) has been known to exist for a long time. This connection is manifested in two forms: the similarity of the intensity profiles in the two spectral domains (e.g. Kundu 1961), and a common flaring loop as the source for both hard x-ray and radio emission, regardless of whether the microwave source is located at the loop top (e.g. Marsh & Hurford, 1980) or at the foot points (e.g. Shevgaonkar & Kundu, 1985). The hard x-ray source is generally at the foot points. Hoyng et al. (1983) described an event observed with SMM, in which they concluded that the microwaves (2 cm wavelength) came from the loop top and the hard x-rays ($\leq$ 32 keV) from the foot points. However, their conclusion cannot be generalized. Prior to the launch of *Yohkoh* there were few published studies of microwave and hard x-ray sources using simultaneously obtained imaging data; the availability of HXT images has increased the number of studies in this area (e.g., Enome et al. 1994; Takakura et al. 1994), but we still have no clear picture of the location of the hard x-ray source relative to the microwave source in a flaring loop.

Sakao (1994; see also Sakao *et al.* 1994) described the nature of hard x-ray emitting electrons in the energy bands 14-23 keV(L), 23-33 keV(M1), 33-53 keV(M2) and 53-93 keV(H) using *Yohkoh*-HXT (Hard X-ray Telescope) imaging data, which has significantly advanced our knowledge in this area. In particular it should be noted that the *Yohkoh*-HXT energy range goes much higher (up to 93 keV) than was the case for the SMM-HXIS instrument or the Hinotori imager. Using this higher energy range ($\geq$ 33 keV) data Sakao (1994) and Sakao *et al.* (1994) were able to characterize the double structure of hard x-ray sources in solar flares. Indeed, Sakao's study provides important information on the source of solar flare hard x-ray emission, the propagation of accelerated electrons in a flaring loop, and the mechanism of acceleration of energetic electrons. Some important findings are: (1) during the impulsive phase, hard X-ray sources are observed on each side of a magnetic neutral line, suggesting that the two sources are the footpoints of a single flaring loop. In fact, they appear to be spatially coincident with the white light brightenings observed with the optical telescope on *Yohkoh*-SXT (e.g., Hudson et al. 1992; Sakao et al. 1992); (2) hard x-ray emission from the two sources varies simultaneously to within 0.1 seconds at the $1\!-\!\sigma$ level, strongly supporting the idea that hard x-rays are emitted from near the footpoints of a flaring loop by energetic electrons streaming downward from near the top of the loop; (3) the footpoint sources often show asymmetry in hard x-ray emission, with the brighter source being located in a weaker magnetic field region than the weaker (or less bright) source. Sakao interpreted the result that the weaker-field footpoint has higher electron precipitation as due to weaker magnetic field convergence, which permits more electrons to reach the chromosphere than at the stronger-field footpoint where magnetic mirroring is stronger.

Sakao determined the field strength at the footpoints of the loop using line-of-sight magnetogram data. Radio imaging data offer a complementary method for testing the proposal that asymmetric hard X-ray precipitation is connected to the differing field strengths at opposite ends of a flaring loop. Radio emission in flares is generally due to nonthermal gyrosynchrotron emission, which has a strong dependence on magnetic field strength. Thus we expect that radio emission from a flaring loop will be strongest at the stronger-field end. For simple events with two footpoints of opposite polarity, we would therefore expect that the radio emission will be brightest at the footpoint which is weakest in hard X-rays. This radio technique complements the determination of footpoint field strengths from overlays on magnetograms, which suffer significant uncertainties due to the difficulty of obtaining simultaneous magnetograms and in carrying out accurate overlays.

Microwave imaging data simultaneous with HXT data, with comparable spatial ($\sim 5''$) and temporal (0.5 sec) resolution, were not available for the HXT events discussed by Sakao. In this paper, we study two radio events observed simultaneously with the HXT experiment and at 17 GHz with the Nobeyama Radioheliograph (NRH). These two events were noticed in the course of another study of the evolution of an active region, and identified as suitable for this study. Both events show structure which is simple enough for us to use them to test whether the connection between radio brightness and hard X-ray brightness is consistent with the asymmetric–loop model.

2. OBSERVATIONS

The two flares under study in this paper were observed on May 28 and May 30, 1993; they originated in AR 7515, which was followed from May 23 to June 2, 1993 as part of a study of active region evolution and flare productivity. We use data from the Nobeyama Radioheliograph (NRH), the Toyokawa and Nobeyama microwave patrol telescopes and the SXT and HXT telescopes on the *Yohkoh* satellite. The properties of these instruments are described below.

The Nobeyama Radioheliograph has been carrying out routine operations since 1992 June. Consisting of eighty–four 80 cm–diameter dishes in a T-shaped array (east-west dimension of 490 m), it can make snapshot images of the whole solar disk with a spatial resolution of order $10''$ every 50 msec (Nakajima et al. 1994). Due to the large number of baselines involved, it is not usually feasible to make images at high time resolution for the whole duration of a flare. Here we use fluxes measured from the maps at selected times, and "fill-in" the time profile with the correlation plots at 1 s time resolution. These consist of the correlation coefficients of visibilities on baselines longer than about 150 m, and thus are insensitive to sources larger than about $24''$. Therefore they do not represent the variation of total power with time; however, in the impulsive phases of the flares we will discuss the source sizes were small and the correlation plots should be a good representation of the total power. We have calibrated the correlation plots in terms of solar flux units by comparison with fluxes obtained from the full radioheliograph in the impulsive phase of the events discussed. These in turn are normalized to a nominal temperature of 10000 K for the quiet solar disk at 17 GHz.

The Toyokawa and Nobeyama patrol telescopes are polarimeters operating at 1.0, 2.0, 3.8, 9.4, 17 and 35 GHz (Torii et al. 1979; Nakajima et al. 1985). The data used here have been processed using new software developed by M. Nishio at Nobeyama.

The *Yohkoh* satellite (Ogawara et al. 1991) is a Japanese satellite carrying joint Japan-US-UK instruments for solar observations. The two instruments which we use are the Soft X-ray Telescope (SXT; Tsuneta et al. 1991) and the Hard X-ray Telescope (HXT; Kosugi et al. 1991). SXT uses grazing-incidence optics to form images on a 1024 x 1024 pixel CCD in the energy range 0.25 - 4 keV; a number of filters can be placed in the optical path. The pixel size is $2.5''$. HXT is a Fourier-synthesis imager consisting of 64 independent subcollimators and forming images in 4 different energy ranges: 14-23, 23-33, 33-53, and 53-93 keV. Spatial resolution is signal-to-noise dependent, but is of order $5''$. *Yohkoh* enters the so-called flare mode when the counting rate of one of its spectrometers exceeds an adjustable threshold. In the flare mode, HXT data from all channels become available; otherwise, only the L-band data are recorded. The flare-mode SXT data usually consist of high-cadence (2s), narrow field-of-view ($2.6'$x $2.6'$) images in three filters, including the two thickest ones in order to measure the temperature of $\sim$ 10 MK flare plasma. These are supplemented with wider field-of-view, reduced resolution images typically once a minute.

In the following two sections we present the observations of the two events separately. All the images displayed are oriented to place solar north at the top of the image. At 17 GHz both flares have an impulsive phase of short duration, $\leq$ 1 min, followed by a post-burst increase phase which lasts a longer period. In the hard x-ray domain, the profiles are both "spiky" and of short duration; the spikiness appears to increase with increasing hard X-ray energy.

3. COALIGNMENT OF HARD X-RAY AND RADIO IMAGES

We first coalign the HXT and SXT images using their coordinates relative to disk center, since the alignment between the two instruments is now well understood (Masuda 1994) and the uncertainty is probably of the order of $1''$. To overlay the radio and X-ray images we make use of the general similarity between Nobeyama and SXT images of the extended active region emission, both of which are produced by thermal bremsstrahlung (Enome et al. 1994). For the 1993 May 30 flare the estimated coalignment accuracy is $3''$. For the 1993 May 28 flare, no SXT image of the whole region was available close to the flare time, except for one at 02:12:58, which has one quadrant empty (SXT was observing AR 7512 during the flare). Alignment for May 28 was carried out using an SXT image at 00:23 UT. The estimated uncertainty is of order $5''$.

4. EVENT OF 1993 MAY 28, 2:02 UT

4.1. Radio and HXR Time Profiles and Energy Spectrum

Figure 1 shows the HXT time profiles at various energy bands. The hard X-ray flare started at $\sim$ 2:02:08 UT in the L band (14-23 keV) while the flare mode was triggered at 2:02:26 UT. For comparison the 17 GHz Nobeyama patrol data are plotted in the bottom panel along with the fluxes measured from radioheliograph images at different times during the flare (crosses). We see two spikes in the HXT L- and M1-band time profiles, peaking at 2:02:47 UT and 2:03:24 UT, respectively (hereafter S1 and S2). While spike S1 is also present in the M2 and H bands, S2 is not clearly seen in these energy bands, suggesting that S2 has a much softer energy spectrum than S1. Assuming a power-law photon incident spectrum, the hard X-ray photon index at around the peak of S1 is $\sim$ 4 while that for S2 is $\sim$ 6 (the ratios M1/L and M2/M1 both give similar results for the indices). The radio data are consistent with S2 having a softer spectrum: at 17 GHz the first peak is much brighter than the second, as would be expected for a harder electron energy spectrum. Note that the fluxes determined from the radioheliograph images are the same as those obtained from the patrol telescopes to within about 20%, which is adequate agreement given the differing techniques involved.

The first peak in the time profile has a shoulder in the L, M1, and M2 bands which becomes less conspicuous in the H-band. This peak S1 also becomes more spiky with increasing HXR energy. This peak corresponds fairly closely in time to the most prominent peak in the microwave domain, to within a few seconds. However, the second peak in L and M1 bands, corresponds to a rather broad peak in the microwave profile.

4.2. Pre-Flare and Flaring Region in Microwaves

At 17 GHz the active region (AR 7515) in which the flare originated consisted of three main bright features in its immediate pre-flare stage (prior to 02:00 UT). Figure 2 shows a representative selection of 17 GHz images of the region and the flare. (This and all subsequent images displayed are oriented with solar north at the top of the image.) The leftmost panels show the preflare region in total intensity (I, upper) and circularly-polarized flux (V, lower). Subsequent images are difference images in which the preflare images have been subtracted: as long as the radio emission is optically thin, which we believe to be the case, this is appropriate. The only significant polarized radio emission in the preflare region lies over a strong sunspot at the western edge of the radio emission (leftmost bottom panel). The flare occurs in the center of the preflare radio source, well away from the leading spot. The second column of panels shows an enhancement at the flare location more than a minute prior to the impulsive phase, at a time when no HXR were detected. This may be evidence for preflare heating. The middle panels, correspond to the rise phase of the flare, show a source elongated NNE-SSW, in which the SSW portion is negatively polarized. At the peak of the flare (fourth column of panels) the northern end of the radio source shows positive polarization; the way in which the positive and negative contours are squashed together in the polarization map indicates that the center of the positively-polarized radio emission is less than 1 beam-width ($\sim 15''$) away from the negatively-polarized emission in the south.

The overall degree of polarization is approximately 10% at the peak of the flare, and is dominated by the negatively polarized emission from the southern portion of the source. The microwave patrol data indicate that the radio spectral peak is close to 10 GHz; from 17 to 35 GHz the radio flux spectral index is -2.3, corresponding to a nonthermal electron energy distribution of index -3.9 in the thick-target model.

4.3. Hard X-ray Source Structure

Hard X-rays were observed with the *Yohkoh*-HXT instrument in all energy bands up to 93 keV. Fig. 3 shows the HXR images at the peak of S1. During the first spike (S1), due to the relatively low count rate, mapping in the M2 band is restricted to the period around the peak (peak count rate 13 cts/s/SC). In the M2 band, we see double sources whose centers are separated by $\sim 23''$, with the north-eastern (NE) source being the brighter. In the L band (and also in the M1 band), the double sources are also clearly seen with again the NE source being brighter than the south-western (SW). The ratio of the peak count rates (SW/NE) is 0.35 in the L band and 0.40 in the M1+M2 bands. The spectral hardness of the NE and SW sources was apparently similar. We suggest that the two sources correspond to footpoints of a single flaring loop. As the flare evolves the images show that the whole loop fills in; this is most pronounced (especially in the L-band) during the valley between the two peaks and at the second peak (not shown). This filling of the loop is probably due to evaporated plasmas produced by the electron bombardment during the first peak.

Figure 3 also shows the 17 GHz contours superimposed on the hard X–ray flare sources. Panels (d) and (e) show the total intensity and polarization of the 17 GHz source, respectively. Note the cospatiality of the HXR footpoint sources with the two oppositely polarized components of the 17 GHz flaring source. The radio emission is much stronger over the weaker hard x-ray footpoint, and extends well south of the hard X-ray emission. No such extension is seen to the north.

4.4. Comparison With Optical Data

No optical data are available at the time of the flare, but magnetograms are available from NAOJ at 00:30 UT, some 2 hours earlier. In Figure 4 we present a number of overlays with optical data. The top left panel has contours of the optical continuum (showing the locations of sunspots) overlaid on the only (partial) SXT frame available for the flare. The top right panel shows HXT contours overlaid on a continuum image; the bottom left panel shows the 17 GHz I contours overlaid on a magnetogram; and the bottom right panel shows the 17 GHz V contours overlaid on the continuum image. The radio images are not preflare-subtracted, so that the coincidence of the polarized active-region emission (westernmost contours, bottom right panel) with a sunspot may be seen. The northern HXT/radio source is very close to a small spot, which, however, does not appear to display strong magnetic fields in the magnetogram. The southern HXT source apparently lies over a narrow tongue of downgoing magnetic field which skirts to the east of a larger, positively-polarized spot. Based on the magnetogram, it is difficult to determine which of the HXT "footpoints" lies over the stronger magnetic field, but their locations are consistent with being on opposite sides of a neutral line.

5. EVENT OF 1993 MAY 30, 6:48 UT

5.1. Radio and HXR Time Profiles and Energy Spectra

This flare shows a simple single-spike time profile in the hard X-ray range peaking at 6:48:54 UT (Fig. 5). There is a gradual increase in hard X-ray flux in the L band from about 6:48:00 UT and the flare mode was triggered at 6:48:46 UT after which data from all four energy bands are available. The time profiles are quite similar in all HXT bands with the burst duration being about 30 s (FWHM) in the L band. There is no significant increase in the H band count rate. The ratio M1/L of HXT energy bands gives a photon spectral index of 3.3 at the flare peak, increasing to about 4 following the peak. The M2/M1 ratio implies a somewhat softer spectrum, with an index of $\sim$ 4.5 throughout the hard X–ray spike. The microwave time profiles are very similar to the hard X-ray profiles. Note that in Fig. 5 the solid line in the microwave panel is the "correlation" data from the radioheliograph, which is not sensitive to large-scale structure, and the divergence between the map fluxes (crosses) and the solid line during the decay of the flare may be due to large-scale emission which is not adequately represented by the correlation data.

5.2. Flaring Region in Microwaves

Like the May 28 event, the May 30, 1993, 06:48 UT event also originated in the active region AR 7515. Prior to the flare the only significant 17 GHz polarization detected is again over a spot in the leading part of the region (Fig. 6). The difference images in this figure show flare emission from a highly elongated (EW) source containing several peaks. Note that the compact source at the eastern end of the region does not change much with time, so we believe that it is not associated with the flare. Throughout the flare the strongest radio emission is at the SW edge of the region, close to but not quite coincident with the polarized sunspot source. The brightest microwave flare source was strongly polarized (negative polarity); the flare emission at the eastern end of the extended radio source is unpolarized.

The strongest radio peak has a degree of polarization steady at about -45% during the impulsive peak. The spectral index for this event from 9.4 to 17 GHz is $\sim$ -2.6, corresponding to a thick-target nonthermal electron distribution of index -4.2.

5.3. X-Ray Source Structure

Figure 7 shows SXT, HXT L and HXT M1 images at the peak of the flare. The SXT image shows several loops, but is dominated by two bright compact features. The HXT images show peaks nearly at the same locations, and also show emission between the bright features as in the SXT images. Panels (d) and (e) of Figure 7 present overlays of the microwave images on the X-ray images. In panel (d) the 17 GHz total-intensity contours are shown superimposed on the SXT image, while in panel (e) the 17 GHz V contours are shown overlaid on the HXT M1 image. As in the previous example, the brightest HXR emission is not coincident with the brightest 17 GHz emission, and the latter probably lies over strong magnetic fields. Since there are more than two hard X–ray sources in this event it is not clear exactly how the topology of the X–ray sources should be interpreted, which is relevant to determining the degree of asymmetry. The westernmost source has about 40% of the count rate of the bright easternmost source in the M1 channel, while the next–to-westernmost source is about 30% of the brightest source.

Unfortunately no simultaneous magnetogram is available and so we are not certain of the location of the photospheric neutral line. We have compared two Kitt Peak magnetograms straddling the time of the flare (May 29 and May 30) with nearly simultaneous SXT images (not shown), and we find that a large spot is close to the X-ray emission in the south–west, whereas no spot is close to the bright source to the north–east. The neutral line crosses between the two brightest X-ray sources, and the magnetic shear across this neutral line appears to be increasing at this time.

The SXT observations reveal four compact areas that brightened in the flare. The compactness and the coincidence with hard X–ray emission in the HXT images argues for their identification as footpoints as opposed to upper parts of loops. Indeed, the brightest soft X-ray source is almost exactly cospatial with the brightest hard X-ray source. Moreover, although the present flare does not show impulsive soft X-ray emission as clearly as the one reported by Hudson et al. (1994), the temporal behavior of the compact SXR sources suggests that they were produced at the same time as the hard X-rays, in contrast to the loop emission which builds up with time due to evaporation from the footpoints. However, we cannot completely rule out the possiblity that each of these compact areas represents the top of a small dense loop. Feldman et al. (1994) argue that soft X-ray emission in a flare tends to be highly localized around the loop top, even in the early phase. In fact a close look at Fig. 7 shows small displacements between soft and hard X-ray sources, which may be due to a height difference between the two sources; the hard X-ray source may represent a footpoint of such a loop where the magnetic field is weaker. In any case, radio observations with the presently available spatial resolution are not sensitive to such fine structures.

6. DISCUSSION

Asymmetry in hard X-ray emission arises via magnetic mirroring in a magnetic loop as follows (e.g., Melrose & White 1979, 1981). Conservation of an adiabatic invariant for an electron gyrating around a magnetic field line means that as an electron propagates towards higher magnetic field strengths, its pitch angle α (the angle between B and the instantaneous velocity of the electron) must increase according to $\sin^2\alpha \propto B$. Consequently, for a particle with a given pitch angle at the top of the loop, there is a maximum field strength to which it can propagate before conservation of adiabatic invariant forces the electron to "mirror" and reverse direction along the field line. If this maximum field strength lies below the chromosphere, then the electron will first strike the dense chromosphere and precipitate. All electrons pass through the lowest-field-strength region, usually assumed to be at the top of the loop. If we consider the velocity distribution of electrons passing through the top of the loop, there is a critical pitch angle such that electrons with smaller pitch angles will precipitate, while electrons with larger pitch angles will mirror in the corona. This critical pitch angle is said to define the "loss cone", i.e., those pitch angles less than the critical value. Particles with pitch angles lying in the loss cone will precipitate at the footpoints of the loop unless they are scattered as they travel along the magnetic field lines. If the field strengths at the feet of the loop differ, then the loss cones for the two feet will also differ in size. In the situation where there is strong pitch–angle scattering in the loop (i.e., on average the particle pitch angle will change by a large amount in traversing the loop), the loss cones will both be filled at all times (since the pitch–angle distribution will be nearly isotropic) and then the ratio of precipitation rates at the two feet (R_1 and R_2) is just the inverse ratio of the field strengths (B_1 and B_2),

$$\frac{R_1}{R_2} \approx \frac{\mathrm{B}_2}{\mathrm{B}_1} \tag{1}$$

(Melrose & White 1979, 1981). The resulting asymmetry in precipitation rates, and hence in hard X–ray emission, can be mild if the two footpoints have similar field strengths.

As mentioned in the Introduction, the asymmetry in the radio emission is a high power of the ratio $\mathrm{B}_1/\mathrm{B}_2$, and thus, unless the asymmetry in precipitation is very strong, the radio emission should be strongest at the footpoint with the weakest hard X–ray emission. This expression only applies to optically–thin gyrosynchrotron emission, but it should generally be valid at 17 GHz which is typically above the spectral peak of flare radio emission. In the optically-thin limit, where radio flux $\mathrm{S} \propto \mathrm{N}_{nt}\mathrm{B}^{0.90\delta-1.22}$ with δ being the spectral index of the electron energy distribution (typically $\delta \approx 4 - 6$) and N_{nt} the number of nonthermal electrons (Dulk & Marsh 1982), the radio fluxes from the two footpoints are in the ratio

$$\frac{\mathrm{S}_1}{\mathrm{S}_2} \propto \left(\frac{\mathrm{B}_1}{\mathrm{B}_2}\right)^{0.90\delta-2.22} \tag{2}$$

for the strong–scattering limit, where we have used (1) to determine the ratio of numbers of nonthermal electrons at the two footpoints. For the typical range $\delta = 3 - 6$, the exponent in

(2) ranges from 0.5 – 3.2. Unfortunately (2) is of little use by itself because of the additional dependence of the radio flux on the angle θ between the line of sight and the magnetic field:

$$\frac{\mathrm{S}_1}{\mathrm{S}_2} \propto \left(\frac{\sin\theta_1}{\sin\theta_2}\right)^{0.65\delta-0.43} \tag{3}$$

The four relevant parameters (B, θ, N_{nt} and δ) required to describe the radio emission completely, and required to evaluate (2) and (3), can be determined at each footpoint if we can measure the radio flux and the polarization of each at two frequencies (e.g., Kundu, Velusamy & White 1987). However, the necessary data are not available for the events we discuss here. Another complication for quantitative analysis is the likelihood that the radio data will be contaminated by emission from weaker–field regions lying along the same line of sight as the footpoint but located higher in the loop.

In the limit of weak pitch–angle scattering in the loop (little change in the particle pitch angle as it traverses the loop), the situation is more complicated. The asymmetry in precipitation is generally much greater than in the strong–diffusion limit because only the particles initially injected into the loss cone for the stronger–field footpoint precipitate at that footpoint: all others, including all particles which are initially outside the loss cones, precipitate at the weaker-field footpoint. However, the particles not initially injected into the loop with pitch angles lying in a loss cone are by definition trapped particles, and it will take some time for their pitch angles to diffuse into the (biggest) loss cone. Therefore the precipitation rates at the two feet at any given instant depend strongly on the history of particle injection into the loop, and there is no simple expression for the instantaneous ratio of precipitation rates in the weak–scattering limit, equivalent to (1) in the strong–scattering limit. Despite the stronger asymmetry in the precipitation and therefore in the hard X–ray emission, the radio emission from the two sides of the loop is expected to be more symmetric than in the strong–diffusion limit. This is because electrons, as they diffuse slowly in pitch angle, bounce between the same magnetic field strength at both ends of the loop until they eventually precipitate at the weaker–field footpoint. Therefore none of the trapped electrons reach the stronger fields in the stronger–field leg of the loop (although the electrons injected directly into the loss cone for that side of the loop do), and symmetry between the two sides of the loop is maintained. With approximate symmetry in the distribution of electrons with magnetic field strength in the two sides of the loop, the asymmetry in the radio emission will be determined largely by the asymmetry in the viewing angle, as in (3). Since comparison of the two footpoints will be most straightforward for events near disk center rather than at the limb, and since the radio source in the stronger–field leg will be higher in the corona and therefore is likely to have a larger value of θ than a source at the chromosphere for such loops, the radio emission is still likely to appear stronger in the stronger–field leg.

How do the two events presented here fit into this picture? In one case bipolar structure with two footpoint sources of opposite polarity was observed at 17 GHz. These oppositely polarized sources observed in the May 28, 1993 event coincide in position with the double “footpoint” sources observed with the HXT experiment in the high energy bands up to M2. For the May 30, 1993 event the 17 GHz flaring source is elongated; it is strong and highly polarized (degree of polarization, 45%) where there are strong magnetic fields but weak hard X–ray emission, and weaker and unpolarized where the hard X–ray emission is strongest. In both events the strongest 17 GHz emission is not coincident with the strongest hard X-ray emission. The May 28 flare may be the first reported identification of a bipolar microwave flaring source with the two polarities co-spatial with the double "footpoints" of the HXR source, as expected in a single-loop flare model.

Thus in both events the radio data are consistent with an asymmetric loop in which the bulk of the precipitation occurs at the footpoint which has the weaker magnetic field strength. In the May 28 flare the data are consistent with a single-loop model; in the May 30 flare both the hard and soft X-ray images show that more than one loop is involved. The magnetogram data for May 28, on the other hand, suggest that the line-of-sight photospheric field strength is strongest near the stronger hard X-ray source. However, this magnetogram also illustrates the difficulties of using overlays on magnetograms to determine the magnetic field strength at a footpoint, since a shift of $5''$ of the HXR sources relative to the magnetogram, which is within the uncertainty of the overlay accuracy, means a very large decrease in the field stength attributed to the northern footpoint. Another effect which is relevant is the inclination of the magnetic field to the line-of-sight. The mirroring effect depends only on the total magnetic field strength at the footpoint. The longitudinal photospheric magnetogram measures the component of B along the line of sight, whereas the radio flux is sensitive primarily to the component of B perpendicular to the line-of-sight. Thus neither is strictly a measure of the mirroring field strength.

7. CONCLUSIONS

Sakao (1994) has concluded that, at least for a small sample of events, the ratio of the count rates in the two components of hard X-ray double-source flares is consistent with an interpretation in which the amount of precipitation at the two feet of a loop is determined by the relative magnetic field strengths at the feet. Sakao's study relied on calculating the photospheric magnetic fields at the hard X-ray footpoint locations. In this study we have used an alternative technique to address the same question: the comparison of hard X-ray and microwave images. The asymmetric loop model predicts that, provided the asymmetry in precipitation is not too strong, the radio emission should be strongest where the magnetic field is strongest, i.e. at the footpoint where hard X-ray precipitation is weakest. That was found to be the case for both events analyzed here. To proceed further and carry out a quantitative analysis of the radio asymmetry, including the role of pitch–angle scattering, requires determination of B, θ, N_{nt} and δ in each footpoint/leg of the radio source. This requires multifrequency data which are not available for these two events.

This type of study relies on having hard X-ray images with enough dynamic range to see both footpoints. Since current hard X-ray images have limited dynamic range, studies of this type must select against cases in which there is a large ratio in precipitation at the two footpoints, e.g., against any situations in which there is a large ratio B_1/B_2, or when there is weak pitch–angle scattering in the corona. In such events it will be difficult to identify the stronger-field footpoint from the X-ray data alone; the addition of radio images may aid in these cases, since we still expect to see a radio source at the stronger field footpoint.

Support for this work at U. Maryland was received from NASA grant NAG–W–1541 and NSF grant ATM 93–16972. This work was initiated while MRK was the guest of the Nobeyama Radioheliograph group and of ISAS.

REFERENCES

Dulk, G. A., & Marsh, K. 1982, ApJ, 259, 350.

Enome, S., & 19 others, 1994, PASJ, 46, L27.

Feldman, U., Sealy, J. F., Doschek, G. A., Strong, K. T., Acton, L. W., Uchida, Y. & Tsuneta, S., 1994, Ap. J., 424, 944.

Hoyng, P. Marsh, K. A., Zirin, H. & Dennis, B. R., 1983, Ap. J., 268, 865.

Hudson, H. S., Acton, L. W., Hirayama, T., & Uchida, Y., 1992, PASJ, 44, L77.

Hudson, H. S., Strong, K. T., Dennis, B. R., Zarro, D., Inda, M., Kosugi, T. and Sakao, T., 1994, Ap. J. Lett., 422. L25.

Kosugi, T. & 11 others, 1991, Solar Phys., 136, 17.

Kundu, M. R., 1961, J. Geophys. Res., 60, 4308.

Kundu, M. R. & Vlahos, L., 1979, Ap. J., 232, 595.

Kundu, M. R., Velusamy, T., & White, S. M. 1987, ApJ, 321, 593.

Marsh, K. A. & Hurford, G. J., 1980, Ap. J. Lett., 240, L111.

Masuda, S, 1994, Ph.D. Dissertation, University of Tokyo.

Melrose, D. B. & White, S. M., 1979, Proc. Astron. Soc. Aust., 3, 369.

Melrose, D. B. & White, S. M., 1981, J. Geophys. Res., 86, 2183

Nakajima, H., & 8 others, 1985, PASJ, 37, 163.

Nakajima, H. & 16 others, 1994, Proc. IEE, 82, 705.

Ogawara, Y. Takano, T., Kato, T., Kosugi, T., Tsuneta, S., Watanabe, T., Kondo, I., & Uchida, Y. 1991, Solar Phys., 136, 1.

Petrosian, V., 1994, in "High Energy Solar Phenomena - A New Era of Spacecraft Measurements", AIP Conf. Proc. 294, eds. J. M. Ryan & W. T. Vestrand, p. 162.

Sakao, T., & 10 others, 1992, PASJ 44, L83.

Sakao, T. 1994, Ph. D. thesis, University of Tokyo.

Sakao, T., Kosugi, T., Masuda, S., Yaji, K., Inda–Koide, M., & Makishima, K. 1994, in "A New Look at the Sun", Proc. Kofu Symp. (eds. S. Enome and T Hirayama), p. 169.

Shevgaonkar, R. K. & Kundu, M. R., 1985, Ap. J., 292, 733.

Takakura, T., & 11 others, 1994, PASJ, 46, 653.

Torii, C., Tsukiji, Y., Kobayashi, K., Yoshimi, N., Tanaka, H., & Enome, S. 1979, Proc. Nagoya University Res. Inst. of Astrophysics, 26, 129.

Tsuneta, S. & 12 others, 1991, Solar Phys., 136, 37.

This preprint was prepared with the AAS LaTeX macros v3.0.

Figure Captions

Figure 1: Hard X-ray time profiles of the 1993 May 28 event from the *Yohkoh* HXT telescope. The upper 4 panels show HXT data in 4 different X-ray energy ranges, as marked; note that data in the three higher energy ranges are not recorded until the count rate in the 14-23 keV channel exceeds a threshold. For comparison, we include the Nobeyama 17 GHz total power (polarimeter) time profile in the bottom panel. The crosses in this panel represent flux measurements from preflare subtracted radioheliograph images.

Figure 2: Contour maps of the 17 GHz radio emission from the 1993 May 28 flare. The upper row of panels shows total intensity maps, and the lower row shows maps of the circularly-polarized flux. The left-most pair of panels corresponds to a preflare time, and these preflare images have been subtracted from the subsequent images in the figure before plotting. The second column of panels is early in the rise phase of the flare, the fourth column is at the peak of the flare, and the last column corresponds to the decay phase. Contour levels are plotted at 4, 8, 12, 16, 20, 30, 40, 50, 75, 100, 150, 200, 300, 400, 600, 800, 1200, 2000, 2800, 3600 and 4000 x 10^3 K (brightness temperature).

Figure 3: Hard X-ray images of the 1993 May 28 flare. Panel (a) is the L-channel (14-23 keV) image from 02:02:44 - 02:02:48; panel (b) is the M1-channel (23-33 keV) image from 02:02:38 - 02:02:44; panel (c) is the M2-channel (33-53 keV) image from 02:02:36 - 02:02:50. The two lower panels show overlays of radio images (contours) on X-ray images (grey-scale). In both panels the X-ray image is the M2-channel (33-53 keV) image from 02:02:36 - 02:02:50. In panel (d) the 17 GHz total-intensity contours from 02:02:46 are overlaid, while in panel (e) the 17 GHz circularly-polarized flux contours from 02:02:46 are overlaid. The field of view is 2.6 arcmin in each frame.

Figure 4: (a) Overlay of optical continuum contours on SXT partial-frame image at 02:12:58 on 1993 May 28. The contours are chosen to show the spot locations in the active region. (b) Overlay of HXT contours, showing the locations of the two hard X-ray sources, on the optical continuum image. (c) Overlay of 17 GHz total intensity map (not preflare-subtracted) on NAOJ magnetogram. (d) Overlay of 17 GHz circular polarization contours on the optical continuum image. The field of view is 5.2 arcmin in each panel.

Figure 5: The hard X-ray light curves of the 1993 May 30 flare (upper 4 panels) in a format identical to Figure 2. The lowest panel shows the 17 GHz light curve based on the Nobeyama 17 GHz radioheliograph data (average of longer baselines).

Figure 6: Radio maps of the 1993 May 30 flare, in the same format as Figure 3.

Figure 7: X–ray images of the 1993 May 30 flare. (a) SXT image (Be filter) at 06:48:59; (b) HXT L band (14-23 keV) image at 06:48:46–49; (c) HXT M1 band (23-33 keV) image at 06:48:46–06:49:02. The two lower panels show overlays of radio images (contours) on X-ray images

(grey-scale). In panel (d) the 17 GHz total intensity contours at 06:48:57 are plotted on the SXT Be–filter image, while in panel (e) the 17 GHz circularly–polarized flux contours are plotted on the HXT M1 image. The field of view is 2.6 arcmin in each frame.

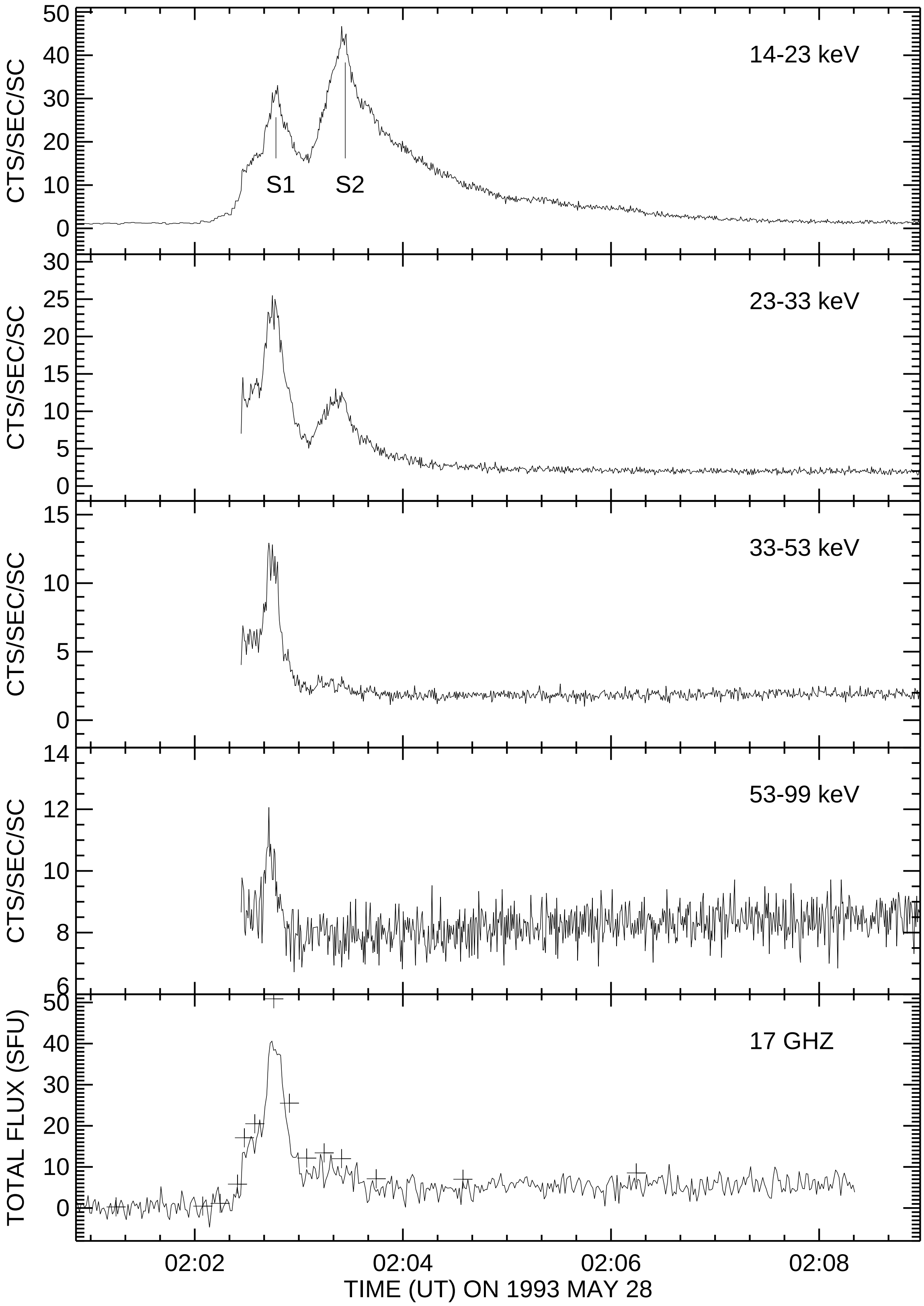

CTS/SEC/SC
50
40
30
20
10
0
14-23 keV
S1
S2
30
25
20
15
10
5
0
23-33 keV
15
10
5
0
33-53 keV
14
12
10
8
6
53-99 keV
TOTAL FLUX (SFU)
50
40
30
20
10
0
17 GHZ
02:02
02:04
02:06
02:08
TIME (UT) ON 1993 MAY 28

Fig. 1.—

Fig. 2.—

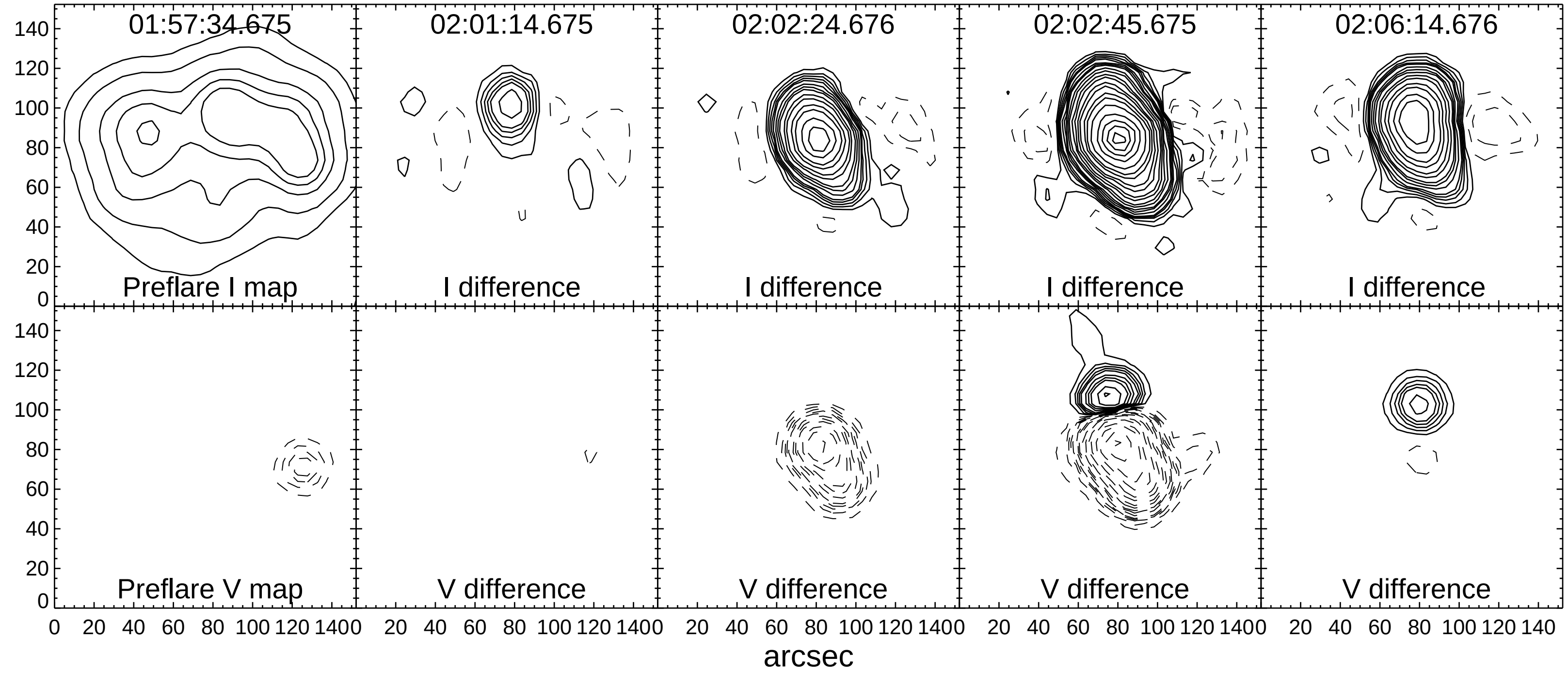

01:57:34.675
02:01:14.675
02:02:24.676
02:02:45.675
02:06:14.676
Preflare I map
I difference
I difference
I difference
I difference
Preflare V map
V difference
V difference
V difference
V difference
arcsec

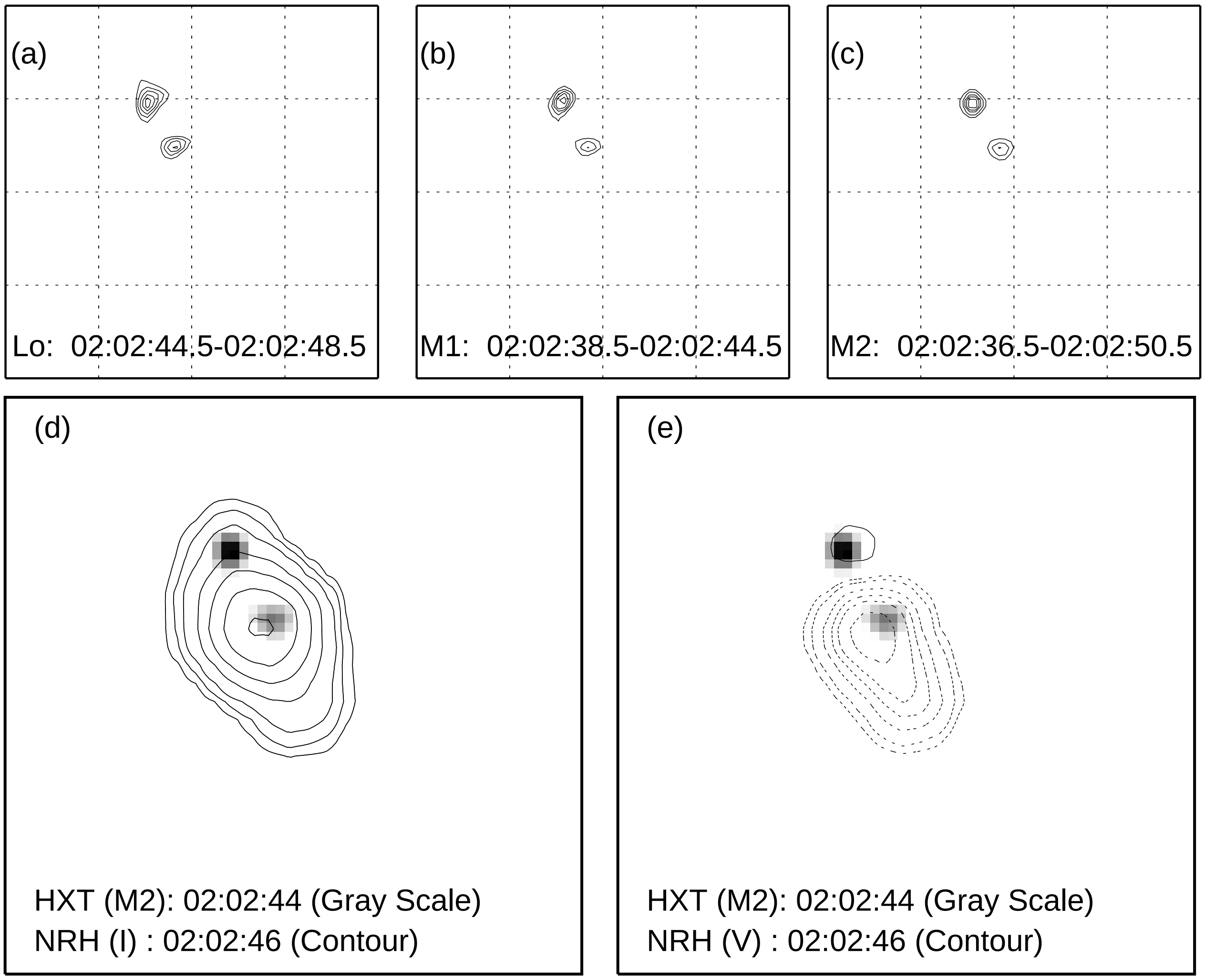
(a)
Lo: 02:02:44.5-02:02:48.5
(b)
M1: 02:02:38.5-02:02:44.5
(c)
M2: 02:02:36.5-02:02:50.5
(d)
HXT (M2): 02:02:44 (Gray Scale)
NRH (I) : 02:02:46 (Contour)
(e)
HXT (M2): 02:02:44 (Gray Scale)
NRH (V) : 02:02:46 (Contour)

Fig. 3.—

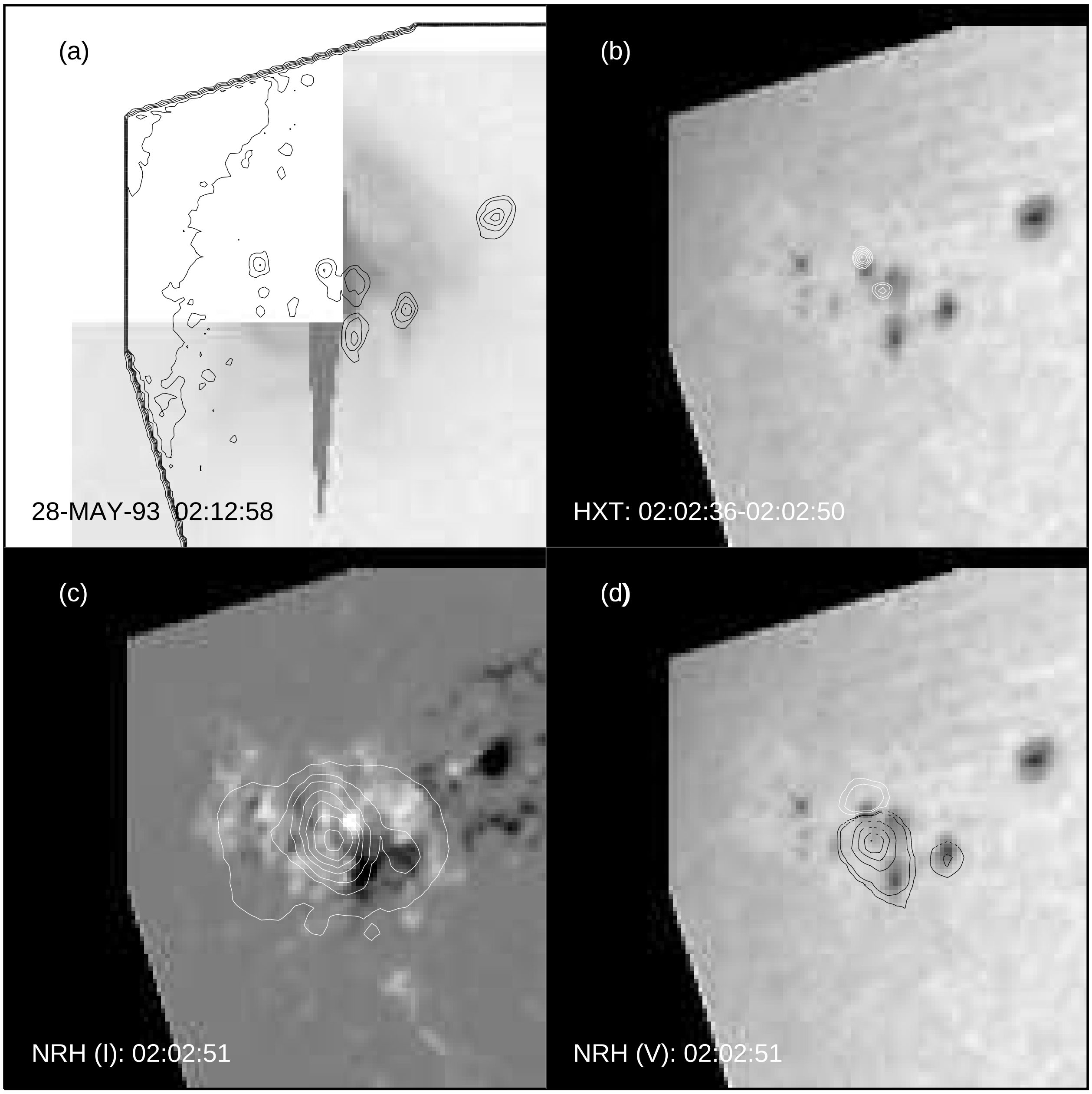
(a)
28-MAY-93 02:12:58
(b)
HXT: 02:02:36-02:02:50
(c)
NRH (I): 02:02:51
(d)
NRH (V): 02:02:51

Fig. 4.—

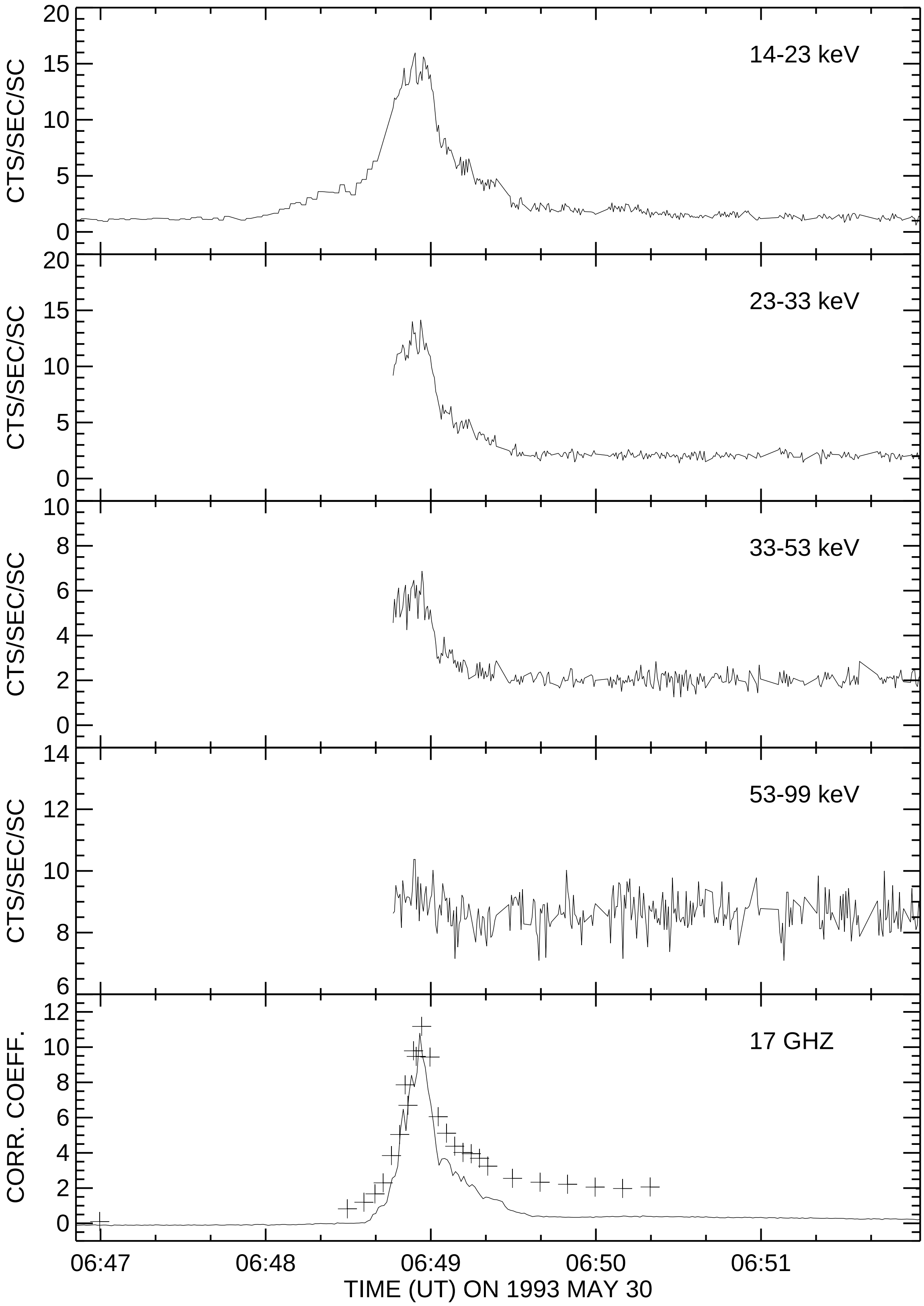
CTS/SEC/SC
14-23 keV
23-33 keV
33-53 keV
53-99 keV
CORR. COEFF.
17 GHZ
06:47
06:48
06:49
06:50
06:51
TIME (UT) ON 1993 MAY 30

Fig. 5.—

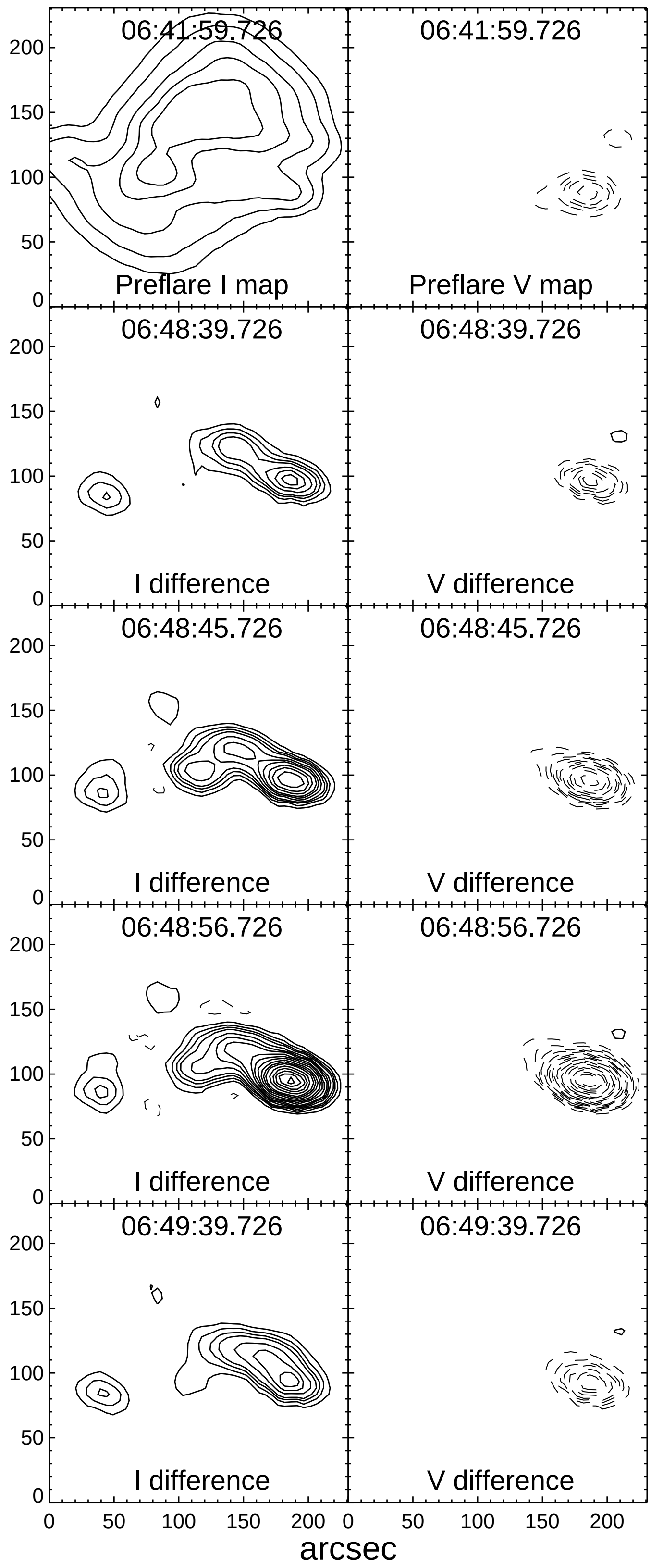
06:41:59.726
Preflare I map
06:41:59.726
Preflare V map
06:48:39.726
I difference
06:48:39.726
V difference
06:48:45.726
I difference
06:48:45.726
V difference
06:48:56.726
I difference
06:48:56.726
V difference
06:49:39.726
I difference
06:49:39.726
V difference
0
50
100
150
200
arcsec

Fig. 6.—

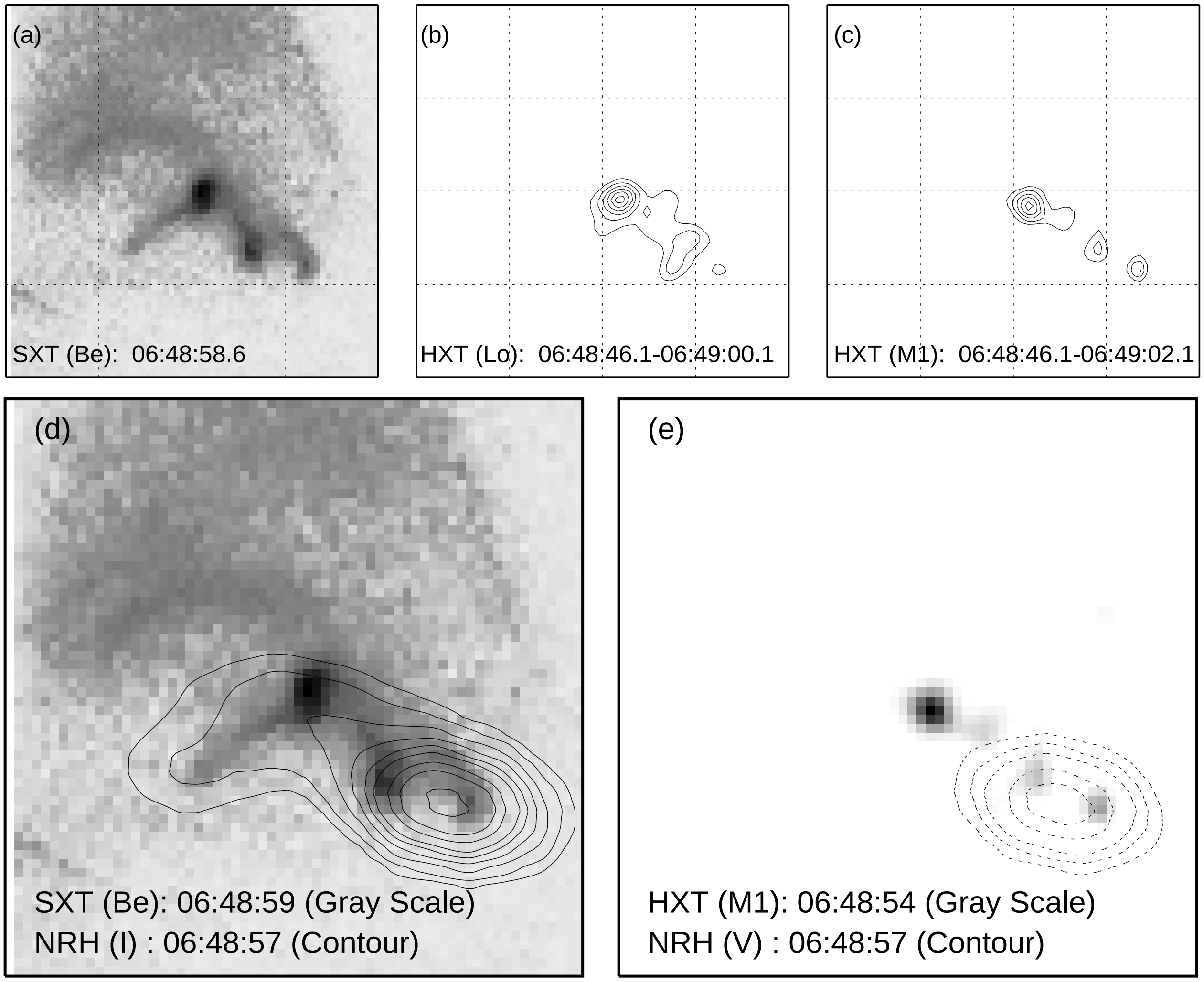
(a)
SXT (Be): 06:48:58.6
(b)
HXT (Lo): 06:48:46.1-06:49:00.1
(c)
HXT (M1): 06:48:46.1-06:49:02.1
(d)
SXT (Be): 06:48:59 (Gray Scale)
NRH (I) : 06:48:57 (Contour)
(e)
HXT (M1): 06:48:54 (Gray Scale)
NRH (V) : 06:48:57 (Contour)

Fig. 7.—